Received: 13 November 2019 | Revised: 28 April 2020 | Accepted: 11 May 2020

DOI: 10.1002/met.1920

RESEARCH ARTICLE

Meteorological Applications RMetS

WRF wind field assessment under multiple forcings using spatialized aircraft data

Federico Carotenuto | **Giovanni Gualtieri** | **Piero Toscano** | **Franco Miglietta** | **Beniamino Gioli**

National Research Council of Italy—Institute for Bioeconomy (CNR IBE), Florence, Italy

Correspondence
Federico Carotenuto, National Research Council of Italy—Institute for Bioeconomy (CNR IBE), Florence Italy.
Email: federico.carotenuto@ibe.cnr.it

Funding information
The research received funding from the European Community's Sixth Framework Programme's project CarboEurope-IP (grant numbers FP6-2002-GLOBAL-1 and GOCE-CT2003-505572) and the European Community's Seventh Framework Programme's project AIRFORS (grant numbers FP7-PEOPLE-2011-IAPP and PIAPP-GA-2011-286079).

Abstract

The performances of limited area weather models are affected by the choice of core solvers, domain resolutions, and initial and boundary conditions. To understand the extent of such differences on simulated wind fields, weather research and forecast (WRF) simulations initialized by different forcings were extensively compared with an aircraft-derived high-resolution data set. The two used forcings were the European Centre for Medium-Range Weather Forecasts (ECMWF) ERA-Interim reanalysis and the National Centers for Environmental Predictions (NCEP) Climate Forecast System Reanalysis (CFSR). The model domain covered a large portion of central western Italy (including part of the Tyrrhenian coast) encompassing the aircraft track and allowed the characterization of their performance across the simulation domain rather than a small set of point-based observations. The WRF results show good agreement with the aircraft data across the whole flight track with both forcings (root mean square errors (RMSEs) < 2.3 $m \cdot s^{-1}$ and an average $r^2 = 0.7$). Orography and coasts show an effect on simulated wind fields. The presence of a strong orography (which is smoothed by the model internal terrain elevation model) is associated with increased errors. Distance from the coast is also associated with a variation in RMSE (even if in a non-straightforward manner) because of potential breeze effects. No forcing data set clearly outperforms the other, while the ECMWF has higher correlation co-efficients when considering wind direction.

KEYWORDS

aircraft observations, CFSRECMWF, modellingwind, WRF

1 | INTRODUCTION

Mesoscale atmospheric models exhibit a growing interest both for scientific and operational use. Among them, the weather research and forecast (WRF) (Skamarock *et al.*, 2008) is today the most adopted of the many different applications. It has been used for weather forecast, being officially adopted by the National Oceanic and Atmospheric Administration (NOAA), and for air quality modelling either when coupled to a chemistry model

(Waked *et al*., 2013) or when integrated with the additional WRF-CHEM chemistry module (Grell *et al*., 2011; Saide *et al*., 2011). The WRF has been also used for various purposes, including wellness and health-related applications (Doherty *et al*., 2009), wind power potential mapping and forecast (Wharton *et al*., 2013; Giannaros *et al*., 2017), wind farm power output assessment (Yuan *et al*., 2017), and as a forcing for Lagrangian particle dispersion models to simulate the atmospheric transport of passive scalars (Nehrkorn *et al*., 2013) and particles (de Foy *et al*., 2011; Bei *et al*., 2013). All these applications are critically dependent on the capability of the WRF to simulate and reproduce the wind speed fields, among other variables, correctly.

State-of-the-art mesoscale models are complex frameworks implementing interrelations and feedbacks between the Earth's biosphere, marine surfaces and atmosphere (Grell *et al*., 1994; Skamarock *et al*., 2008). Simulation outputs strongly depend on model parametrizations and settings, in terms of the initialization data set (i.e. forcing), surface scheme, cloud scheme, land-use data, digital terrain model, and so on. The optimal choice of such parametrizations is not universal but depends on the variable of interest. Specifically, several components of the WRF are related to wind speed fields, such as the land surface scheme that contains the parametrization of mass and energy exchanges between the surface and the planetary boundary layer (PBL), and the PBL parametrization itself. Santos-Alamillos *et al*. (2013) reported that wind speed and direction estimates were mostly influenced by the PBL scheme and, particularly for wind direction, by orography. Giannaros *et al*. (2017) highlighted a tendency of the WRF to overestimate weak winds and to underestimate strong winds, with the highest biases being related to the parametrization of complex topography. Wharton *et al*. (2013) highlighted the importance of optimal surface and PBL schemes to improve the surface–atmosphere exchange simulations and therefore the wind speed vector estimation across the PBL.

The presence of complex orography is among the factors influencing the discrepancy between measured and simulated wind fields (e.g. Giannaros *et al*., 2017). Mesoscale models represent the land surface at a coarse resolution, which may lead to discrepancies between simulated wind speed and measurements from ground stations located at certain altitudes (Carvalho *et al*., 2014). Orographic-induced biases were also found by García-Díez *et al*. (2015) in a comparison experiment with the WRF forced by the European Centre for Medium-Range Weather Forecasts (ECMWF) ERA-Interim reanalysis, National Centers for Environmental Predictions (NCEP)-National Center for Atmospheric Research (NCAR) reanalysis, and the NCEP Global Forecast System (GFS) (Yang *et al*., 2006).

However, all these studies compared model data at the finest grid horizontal resolution, that is, typically between 1 and 5 km, with point-based ground observations close to the surface, and they used a single specific forcing data set as initial and boundary conditions (Jiménez *et al*., 2013; Jiménez and Dudhia, 2013; Santos-Alamillos *et al*., 2013; Yang *et al*., 2013; Draxl *et al*., 2014). Moreover, point-based ground measurements, unless very dense networks are deployed, provide a limited assessment of wind spatial variability, which instead is very important when used to evaluate the model's capability to simulate atmospheric circulations.

Light aircraft (Gioli *et al*., 2006) and unmanned aerial vehicles (Reuder *et al*., 2012) are important data sources for environmental and atmospheric studies, especially in sounding the surface–atmosphere interface and the PBL. These platforms allow researchers to cover horizontal scales from a few metres to hundreds of kilometres, and to perform vertical profiling from the surface up to several kilometres. The past 20 years have seen the development of high-sensitivity and high-frequency probes and their associated processing algorithms that give aerial platforms the capability to measure surface fluxes of momentum and passive scalars (Miglietta *et al*., 2007; Toscano *et al*., 2011), and the wind vector at high spatial resolution (Kocer *et al*., 2011; Mayer *et al*., 2012; Thomas *et al*., 2012; Bonin *et al*., 2013), providing novel data to assess the models' performance in both space and time.

This study is therefore focused on the assessment of the WRF's capability to simulate mesoscale wind speed and direction based on two different forcing data sets with different spatial resolutions. The two used forcings were the ECMWF ERA-Interim reanalysis (Simmons *et al*., 2007; Dee *et al*., 2011) and the NCEP Climate Forecast System Reanalysis (CFSR) (Saha *et al*., 2010). Such an assessment is made by comparing model outputs with extensive aircraft measurements over a regional domain. The study area covers a large portion of central western Italy (Tuscany) extending from the coastline to about 100 km inland, covering the main land-use classes and various orography conditions. The aircraft data set is rather unique because it offers repeated measurements over a span of two years, therefore covering seasonal variability. Model performance could be assessed: (1) in terms of temporal and spatial variability; (2) along terrain height variations that are critical in mesoscale

atmospheric modelling (Carvalho *et al*., 2014); and (3) in terms of the capability to simulate local-scale circulations, such as the sea breeze that develops along the transition from the sea to inland areas.

2 | DATA AND EXPERIMENTS

2.1 | WRF model set-up

The WRF is a mesoscale numerical weather prediction system that employs a fully compressible, Euler non-hydrostatic equations set (Skamarock *et al*., 2008). The model uses a terrain-following, dry hydrostatic-pressure vertical co-ordinate and an Arakawa staggered C-grid as horizontal co-ordinates. The WRF system contains two dynamic solvers to perform time and space integration of the motion equations. Version 3.5.1 of the Advanced Research WRF (ARW) solver was used. The model was set up with the following parametrizations on the basis of Mohan and Bhati (2011) and Santos-Alamillos *et al*. (2013): the Morrison 2 Moment scheme (Morrison *et al*., 2009) for cloud microphysics; the Rapid Radiative Transfer Model (RRTM) scheme (Mlawer *et al*., 1997) for long wave radiative transfer; the Rapid Radiative Transfer Model for Global Circulation Models (RRTMG) scheme (Iacono *et al*., 2008) for short wave radiative transfer; the Revised MM5 Surface scheme (Jiménez *et al*., 2012) for surface parameterization; the Unified NOAH Land Surface Model for land surface parameterization (Ek *et al*., 2003); and the Yonsei University scheme (Hong *et al*., 2006) for PBL parameterization (Table 1).

Land use was provided by the moderate resolution imaging spectroradiometer (MODIS) classes implemented in the WRF (at 30 arcsec resolution) with the NOAH land surface model for surface parameterization. The MODIS-derived static land-use data set is classified into 20 land-use categories with a single category for the urban/built-up environment: one for croplands, one for a mosaic of cropland/natural vegetation, and the others divided between various types of natural environments (different types of forest, savanna, tundra, and so on). Two different sets of initial and boundary conditions were provided every 6 hr (at 0000, 0600, 1200 and 1800 UTC), characterized by different spatial resolutions: ECMWF ERA-Interim data have a resolution of 0.75°, while CFSR data have a resolution of 0.5° (pressure-level variables) and 0.3° (surface data). For further information about raw reanalysis data, see Supporting Information. The modelled domain was divided vertically into 35 eta levels. All simulations were run with a spin-up time of 24 hr. Three nested domains were simulated with a 3:1 ratio between them, reaching a resolution of 3 km in the innermost domain (85 × 74 grid points) covering the region spanned by the flights (Figure 1). The two WRF runs using the two forcing data sets are named throughout as WRF-ECMWF (the simulation forced by the ERA-Interim) and WRF-CFSR (the simulation forced by the NCEP-CFSR). For both configurations, the model was run for 16 intensive observation periods (IOPs) between 2004 and 2005 (Table 2).

TABLE 1 Weather research and forecast (WRF) configuration

Physics module	Chosen scheme
Cloud microphysics	Morrison 2 Moment scheme (Morrison *et al*., 2009)
Long wave radiation	Rapid Radiative Transfer Model (RRTM) scheme (Mlawer *et al*., 1997)
Short wave radiation	Rapid Radiative Transfer Model for Global Circulation Models (RRTMG) scheme (Iacono *et al*., 2008)
Surface layer	Revised MM5 scheme (Jiménez *et al*., 2012)
Land surface	Unified NOAH Land Surface Model (Ek *et al*., 2003)
Planetary boundary layer	Yonsei University scheme (Hong *et al*., 2006)

2.2 | Digital elevation model (DEM)

The WRF internal DEM was compared with the high-resolution Advanced Spaceborne Thermal Emission and Reflection Radiometer (ASTER) global DEM v.2 (GDEM2),[1] which is a product of the Japan Ministry of Economy, Trade and Industry (METI) and the US National Aeronautics and Space Administration (NASA) in order to evaluate better the orographic effects on model outputs. The ASTER data set is composed of a matrix of 22,702 tiles covering from 83° N to 83° S and it has a grid resolution of approximately 30 m (Tachikawa *et al*., 2011).

2.3 | Aircraft platform

The Sky Arrow ERA platform was used for all flights in the study: it carried a mobile flux platform (MFP) capable of measuring three-dimensional wind and turbulence along with H_2O and CO_2 densities as well as other atmospheric parameters (Gioli *et al*., 2006). Wind measurements were made with the Best Available Turbulence (BAT) probe (Crawford and Dobosy, 1992), whose nine-hole hemispheric pressure sphere measured the velocity of the air with

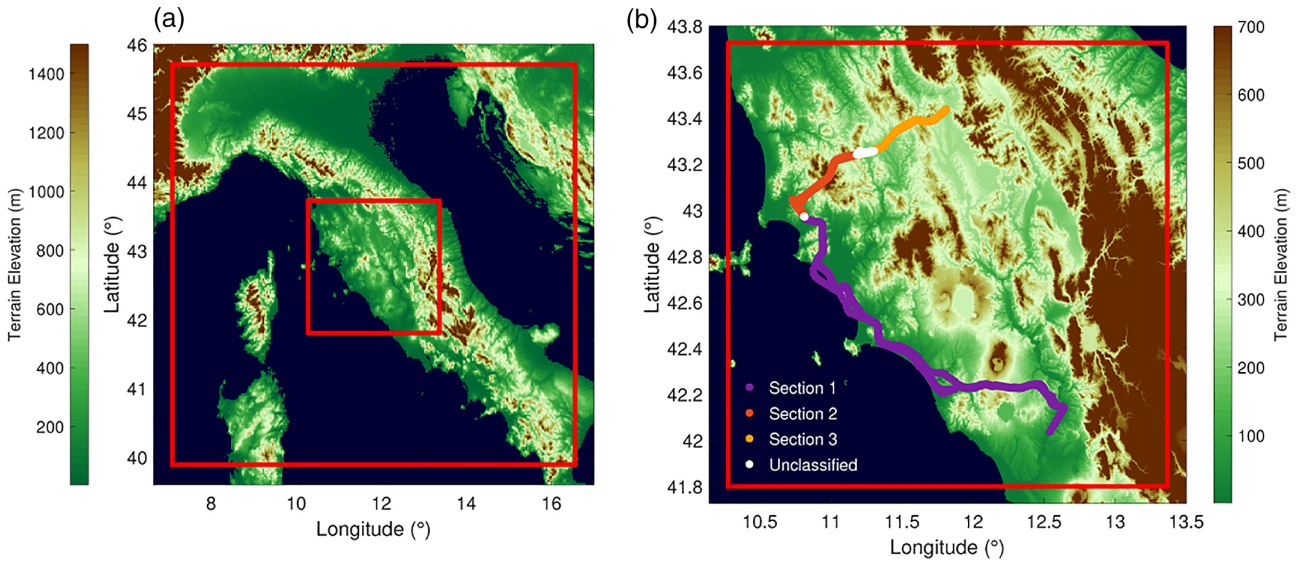

FIGURE 1 Study and simulation area: (a) nested domains of the weather research and forecast (WRF) simulations (red squares); and (b) the innermost simulation nest (red square) and aircraft tracks. For (b), the colour of the track indicates the respective section: 1: purple; 2: deep orange; 3: light orange/yellow; and the tracks not pertaining to a specific section: white. In both (a) and (b), the ground elevation (colour bar; blue is for water) is also indicated

TABLE 2 Analysed intensive observation periods (IOPs)

IOP no.	Period	Flight times (UTC)	Total time (hr)
1	July 21–22, 2004	0900–1809	14
2	August 9–11, 2004	0841–1546	18
3	August 24–25, 2004	0925–1614	19
4	November 16–18, 2004	0910–1617	14
5	December 7–8, 2004	1000–1620	15
6	December 21–23, 2004	0933–1622	14
7	January 12–14, 2005	1014–1536	10
8	March 16–18, 2005	0932–1614	17
9	April 5–14, 2005	0840–1611	15
10	May 3–10, 2005	0826–1721	23
11	July 12–13, 2005	0841–1800	20
12	July 27–29, 2005	0849–1844	20
13	August 31–September 2, 2005	0842–1818	22
14	September 21–23, 2005	0859–1623	22
15	October 24–26, 2005	1129–1537	18
16	December 14–16, 2005	1008–1634	14

respect to the aircraft. The actual wind components (u, v and w) were then evaluated by removing the three-dimensional aircraft motion. The latter is measured by global positioning satellite and inertial navigation system units coupled to accelerometers covering both low- and high-frequency velocity variations over all the aircraft's six degrees of freedom. For a description of the MFP data processing and calibration procedure, see Vellinga *et al.* (2013). Finally, the aircraft also mounted a laser altimeter (LD-90, RIEGL Laser Measurement Systems, Horn, Austria) to measure the flight altitude above the ground.

2.4 | Study area and aircraft measurements

The study area covers parts of the Tuscany and Lazio regions, containing 240 km of flight tracks that were

designed to be representative of the whole area in terms of land use, orography and meteorological conditions (Figure 1b). The region's climate is typically Mediterranean, with mean annual rainfall between 700 and 1,000 mm and average annual temperature around 14–16°C. According to the Corine Land Cover 2006 classification (ISPRA, 2010) the flight area is dominated by forest and agricultural land. The orography is generally flat on the coast and becomes more variable moving from the southwest to the northeast inner area, reaching a peak altitude of 600 masl, while the final inland part is moderately hilly (Gioli *et al*., 2014). The experimental plan for the flights, originally designed for measuring carbon fluxes at a regional scale for the CARBIUS project (Maselli *et al*., 2010), was based on a set of IOPs in different seasons of the year, over a repetitive path and in different times of the day, therefore sampling both spatial and temporal variability. The flights were made between July 2004 and December 2005 for a total of 16 IOPs (Table 2). Flights were made well within the PBL, with altitudes recorded by the laser altimeter from 59 to 346 m, with an average of 135 ± 40 m.

The data set was partitioned by season and by land characteristics to assess the error sources between model and aircraft data across different temporal and spatial patterns. Three main flight sections were defined: (1) a coastal area (characterized mainly by flat agricultural areas and small spots of forested areas with a slightly higher elevation); (2) a more pronounced orography covered almost exclusively by forests and semi-natural lands; and (3) a section mainly characterized by both agricultural areas, forests and semi-natural areas, and a relevant orography (Figure 1b).

The IOPs were also divided by season: winter (December–February), spring (March–June), summer (July–September) and autumn (October–November).

2.5 | Data: Model comparisons

Aircraft and model data were processed to account for the different spatial and temporal resolution using the following workflow.

2.5.1 | Aircraft and model data match

Aircraft wind data were collected at 50 Hz, which corresponds to a horizontal resolution of about 80 cm considering an average aircraft speed of 40 $m \cdot s^{-1}$. Data were spatially averaged into 1.5 km segments to be comparable with the resolution of the innermost WRF domain (3 km). Each flight segment was then associated with the closest WRF grid cell. Similarly, temporal alignment was obtained by matching the UTC time of each flight segment with the temporally closest WRF timestamp. The WRF altitude data were converted to geopotential height (height above mean sea level—AMSL) to be comparable with aircraft data.

Wind speed was calculated (for both the WRF and aircraft data) from u, v and w velocity components. Since the WRF employs a staggered grid where the u, v and w components are located on cells' borders, they were reported to the cells' centre point *via* a destaggering process. This allowed a unique position for each cell to be obtained, which was then used to perform the model–aircraft matching.

2.5.2 | Measures of goodness of fit

Several metrics were computed to assess the agreement between model and aircraft wind speed data (following Santos-Alamillos *et al*., 2013):

$$\text{Root mean square error (RMSE)} : \sqrt[2]{\frac{\sum_i (m_i - o_i)^2}{N}} \quad (1)$$

$$\text{Relative standard deviation (RELSD)} : \frac{\sqrt[2]{N\sum_i (m_i - o_i)^2}}{\sum_i o_i} \times 100 \quad (2)$$

$$\text{Bias (BIAS)} : \frac{\sum_i (m_i - o_i)}{N} \quad (3)$$

$$\text{Relative bias (RELBIAS)} : \frac{\sum_i (m_i - o_i)}{\sum_i o_i} \times 100 \quad (4)$$

where N is the number of values; and m_i and o_i are the modelled and observed wind speeds.

Wind direction, which is a circular variable, was assessed by computing the Pearson correlation coefficient (5) between wind direction distribution frequencies:

$$\rho_{wd} = \frac{\text{cov}(H_m, H_o)}{\sigma(H_m) \times \sigma(H_o)} \quad (5)$$

where ρ_{wd} is the wind direction frequency correlation; and H_m and H_o are the wind direction frequencies for the model and observation, respectively. Wind direction

histograms were computed using 36 bins, each 10° wide. Essentially, this represents a frequency correlation smoothed on 10°′ bins. This frequency correlation allowed the strength of the relationship to be analysed in a trend-wise term when accounting for data circularity.

3 | RESULTS

3.1 | Data overview and overall comparisons

An overview of the simulations' results over all the IOPs combined is presented in Figure 2 for both wind speed (Figure 2a) and wind direction (Figure 2b). The average wind speed measured by the aircraft over all the IOPs is 4.18 ± 0.02 m·s^{-1} (95% confidence interval of the mean), while both the WRF-ECMWF and the WRF-CFSR report comparable, but higher, means (4.51 ± 0.02 and 4.71 ± 0.02 m·s^{-1}, respectively). Overall, the WRF outputs (for the innermost 3 km domain) show good agreement with the aircraft data (Table 3) for the estimation of wind speed (average RMSE with the two forcings = 2.22 m·s^{-1}). Frequency distributions of wind direction data reveal non-univocal differences between observations and model outputs. Aircraft wind direction (Figure 2b) shows three main peaks: one in the northnortheast sector (between 15 and 45°), another in the southern sector (between 165 and 195°), and finally a smaller one between 255 and 270°. Model data tend to follow the same peaks: northerly peaks are higher than the aircraft's (average relative frequency across models = 7.17% ± 0.05% *versus* 5.23% ± 0.65% for the aircraft), while the second peak has a more complex composition. Between 165 and 180° the WRF-ECMWF has higher frequencies than the aircraft (5.88% ± 0.70% *versus* 5.48% ± 0.28%), while the WRF-CFSR shows lower frequencies. In the 195° bin, the WRF-ECMWF shows lower frequencies, while the WRF-CFSR overshoots. The third peak is where model data follow more closely the aircraft frequencies with only a slight over- or underestimation. In general, both the WRF-ECMWF and the WRF-CFSR are quite able to follow the frequency trend of the observed data. The histogram correlation co-efficients for 10° binned wind direction are 0.84 for the WRF-ECMWF and 0.81 for the WRF-CFSR.

3.2 | Data partitioning: Sections and seasons

Statistics for the data partitioning described in Section 2.4 (for both wind speed and direction) are reported in Table 3. The average wind speed RMSE across sections is 2.19 ± 0.08 m·s^{-1} for the WRF-CFSR and 2.27 ± 0.11 m·s^{-1} for the WRF-ECMWF. Similarly, the average wind speed RMSE across seasons is 2.17 ± 0.57 m·s^{-1} for the WRF-CFSR and 2.19 ± 0.6 m·s^{-1} for the WRF-ECMWF. Overall,

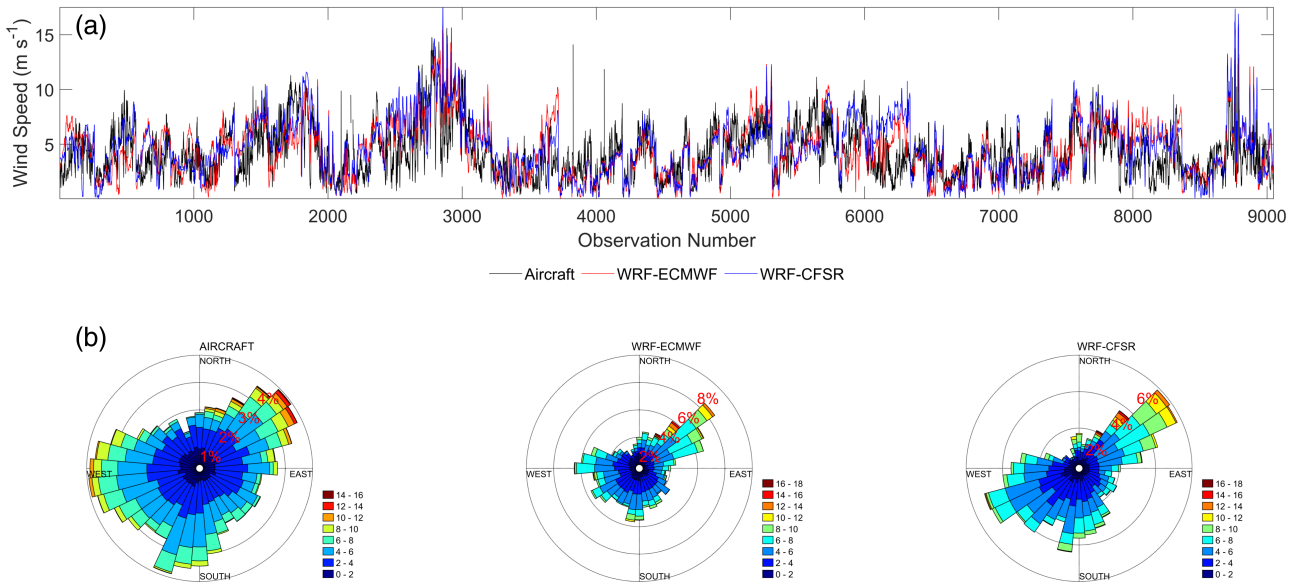

FIGURE 2 Global plots of the innermost domain weather research and forecast (WRF) data *versus* aircraft data: (a) wind speed; and (b) wind direction. A solid black line indicates aircraft data; a solid blue line indicates the WRF forced by the Climate Forecast System Reanalysis (CFSR) (WRF-CFSR); a solid red line the WRF forced by the European Centre for Medium-Range Weather Forecasts (ECMWF) (WRF-ECMWF). In (b) each wind rose represents either the aircraft or a model as indicated by the label

TABLE 3 Summary of statistics for data partitions.

WRF-ECMWF	Section			Season			
Wind speed	**1**	**2**	**3**	**1**	**2**	**3**	**4**
RMSE ($m \cdot s^{-1}$)	2.390	2.216	2.199	3.031	1.836	2.225	1.680
RELSD (%)	50.273	51.768	65.891	64.193	42.668	55.145	46.922
BIAS ($m \cdot s^{-1}$)	0.018	0.537	0.522	1.263	−0.359	0.399	0.109
RELBIAS (%)	0.372	12.546	15.626	26.748	−8.353	9.889	3.039
Wind direction	1	2	3	1	2	3	4
ρ_{wd}	0.841	0.614	0.742	0.844	0.846	0.689	0.600
	1	2	3	1	2	3	4
Observations	3,257	3,249	2,162	1,665	2,249	4,198	936
WRF-CFSR							
RMSE ($m \cdot s^{-1}$)	2.277	2.178	2.124	3.009	1.776	2.077	1.821
RELSD (%)	47.890	50.863	63.625	63.728	41.264	51.491	50.864
BIAS ($m \cdot s^{-1}$)	0.368	0.697	0.549	1.579	−0.228	0.592	0.263
RELBIAS (%)	7.741	16.291	16.458	33.452	−5.292	14.663	7.352
Wind direction	1	2	3	1	2	3	4
ρ_{wd}	0.697	0.641	0.742	0.801	0.805	0.774	0.525
	1	2	3	1	2	3	4
Observations	3,257	3,249	2,162	1,665	2,249	4,198	936

Note: Sections correspond to the three different flight sections as described in the main text. Seasons are: winter (1; December–February), spring (2; March–June), summer (3; July–September) and autumn (4; October–November). For abbreviation/definitions, see the text.

the WRF tends to overestimate wind speed regardless of the used forcing and shows a marked drop in wind direction correlation in geographical section 2, which has the higher terrain elevation.

The WRF-ECMWF and WRF-CFSR are quite comparable in terms of the RMSE, with the WRF-CFSR showing smaller RMSEs both when partitioned over different spatial sections and in different seasons (with the exception of autumn). Instead, the WRF-ECMWF shows smaller biases (with the exception of spring).

For wind direction, a seasonal effect is present: the frequency correlation decreases in summer and even more in autumn for both forcings, suggesting a mesoscale systematic effect affecting circulations.

3.3 | Temporal partitioning: Diurnal courses

The capability of the different forcings to reproduce wind speed variability over time is assessed by exploring the strength of the linear correlation (expressed as the square of the Pearson correlation co-efficient, r^2) between model data and observations' hourly diurnal courses (Figure 3) divided by season and flight section. Overall, the WRF-CFSR is better correlated with aircraft data, with the notable exception of section 2 (Figure 3b, e, h and k), where the WRF-ECMWF forcing has a higher r^2 in all seasons. Section 2 is also the area where the lowest r^2 were registered in autumn, when values for all the models drop very close to zero.

3.4 | Spatial Partitioning: Across-sections analysis

A further spatial analysis was made by computing the cumulative flight covered distance from a fixed origin, and averaging wind speed along such distance on both geographical sections and seasons (Figures 4–7). Both the WRF internal DEM and ASTER DEM profiles were shown to assess the elevation smoothing in the coarser WRF internal DEM. Furthermore, the r^2 and RMSE were calculated *per* each section and season.

All data sets show a decrease in performance in summer (with r^2 always < 0.38), and section 3 reported the lowest r^2 for all data sets. In summer, the WRF with both

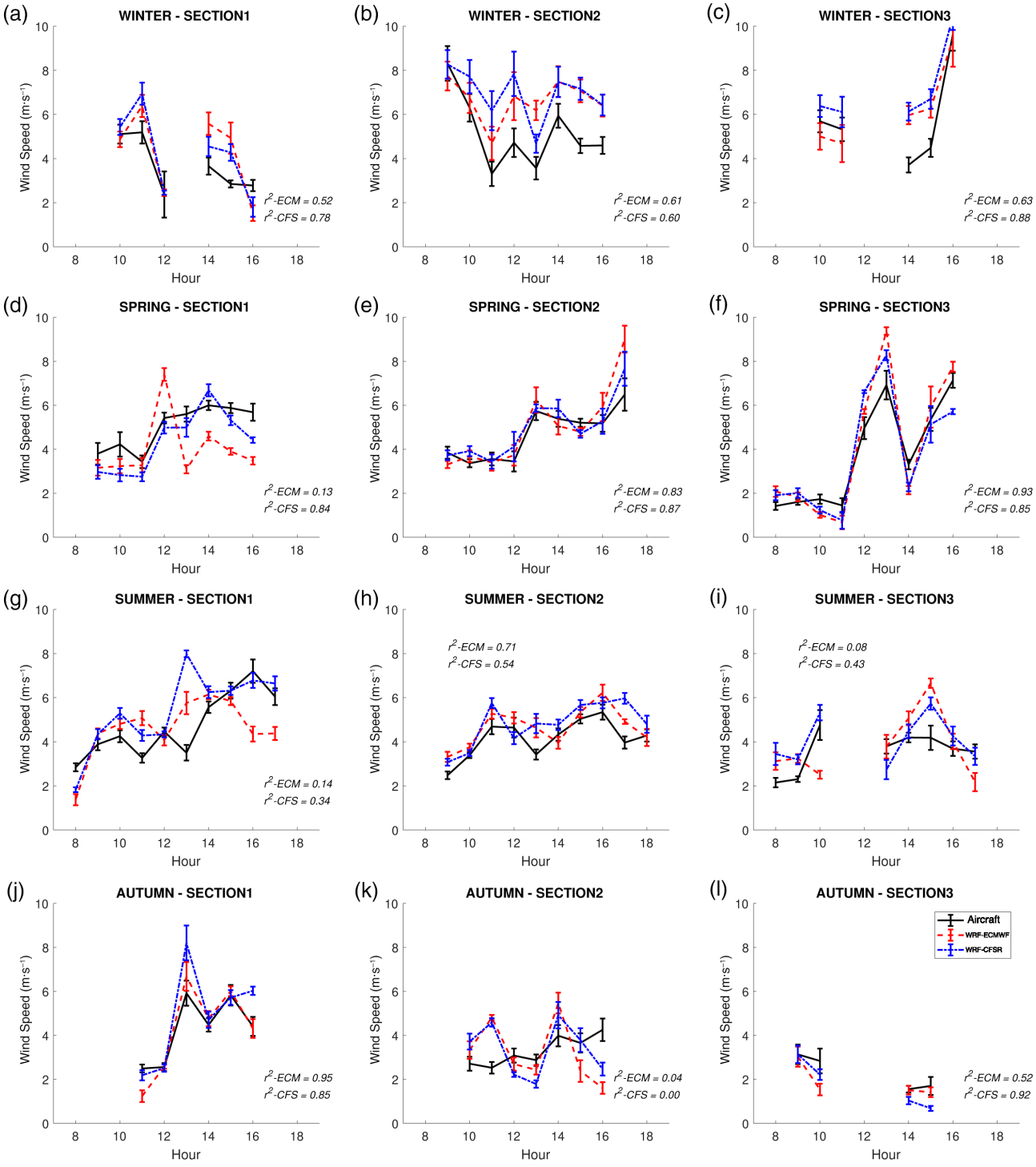

FIGURE 3 Diurnal courses for the wind speed for aircraft and simulated data aggregated for different seasons and flight sections: (a–c) sections 1–3 for winter; (d–f) sections 1–3 for spring; (g–i) sections 1–3 for summer; and (j–l) sections 1–3 for autumn. Black solid lines indicate aircraft data; blue dash-dotted lines indicate the weather research and forecast (WRF) forced by the Climate Forecast System Reanalysis (CFSR) (WRF-CFSR); and red dashed lines the WRF forced by the European Centre for Medium-Range Weather Forecasts (ECMWF) (WRF-ECMWF). Error bars indicate the standard error for each hour. The plots also indicate the co-efficients of determination for both the WRF-ECMWF (ECM) and the WRF-CFSR (CFS)

forcings tends to overestimate the measurements along the whole track, hinting at a spatial-independent seasonal effect. The different seasonal performances in section 1 (i.e. coastal section) can also be explained with the existence of a breeze regime, which is investigated in Figure 8a–d, where the mean RMSEs for wind speed are

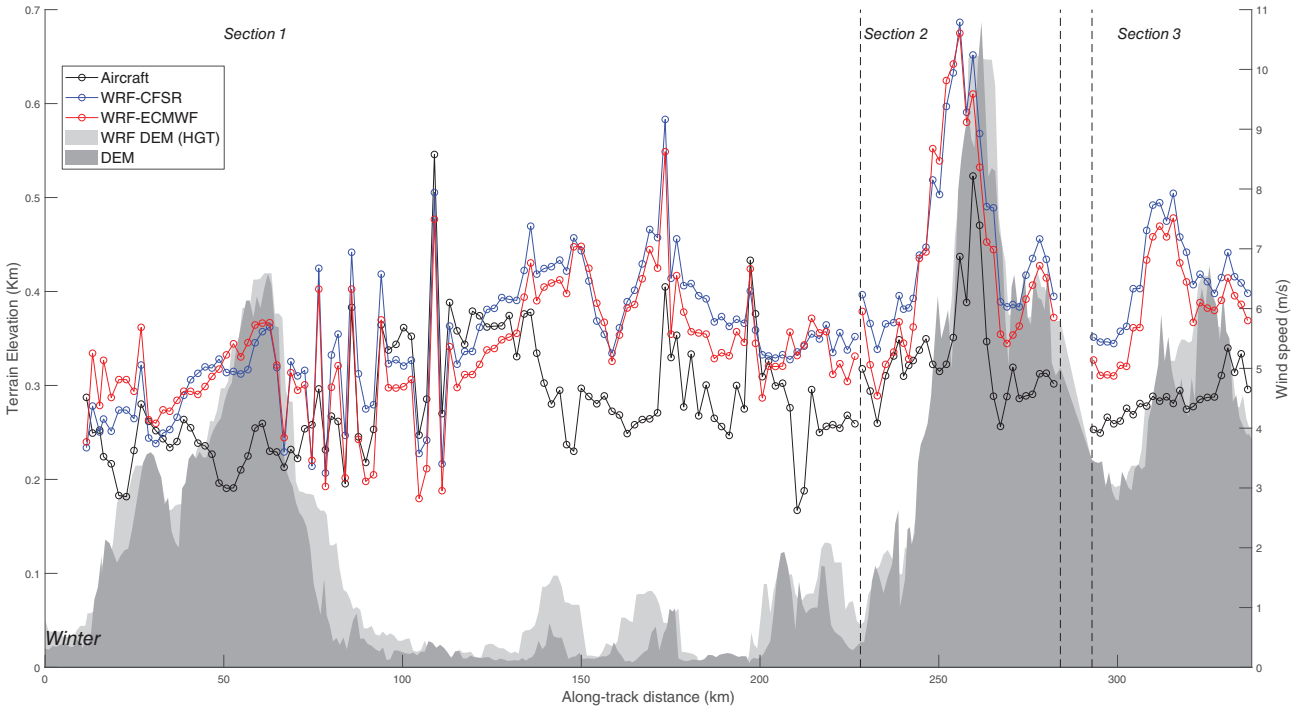

FIGURE 4 Spatialized wind speed for winter (season 1). Each solid line with circles indicates the wind speed (right *y*-axis) for a different data set: Aircraft (black), weather research and forecast (WRF) forced by the European Centre for Medium-Range Weather Forecasts (ECMWF) (WRF-ECMWF) (red) and the WRF forced by the Climate Forecast System Reanalysis (CFSR) (WRF-CFSR) (blue). Dark grey areas indicate terrain elevation (left *y*-axis) as *per* the Advanced Spaceborne Thermal Emission and Reflection Radiometer (ASTER) GDEM2, while the light grey areas show the WRF's own digital elevation model (HGT). Dashed black lines separate the sections

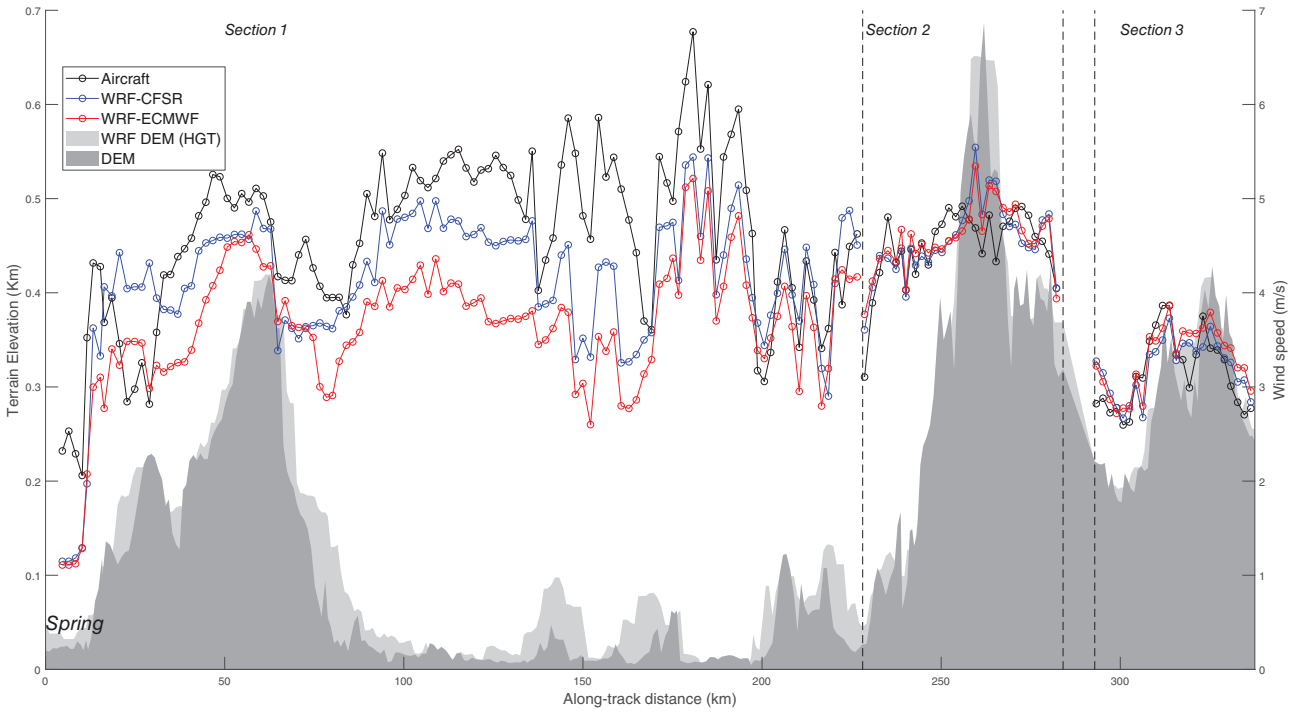

FIGURE 5 Spatialized wind speed for spring (season 2). Each solid line with circles indicates the wind speed (right *y*-axis) for a different data set: Aircraft (black), weather research and forecast (WRF) forced by the European Centre for Medium-Range Weather Forecasts (ECMWF) (WRF-ECMWF) (red) and the WRF forced by the Climate Forecast System Reanalysis (CFSR) (WRF-CFSR) (blue). Dark grey areas indicate terrain elevation (left *y*-axis) as *per* the Advanced Spaceborne Thermal Emission and Reflection Radiometer (ASTER) GDEM2, while the light grey areas show the WRF's own digital elevation model (HGT). Dashed black lines separate the sections

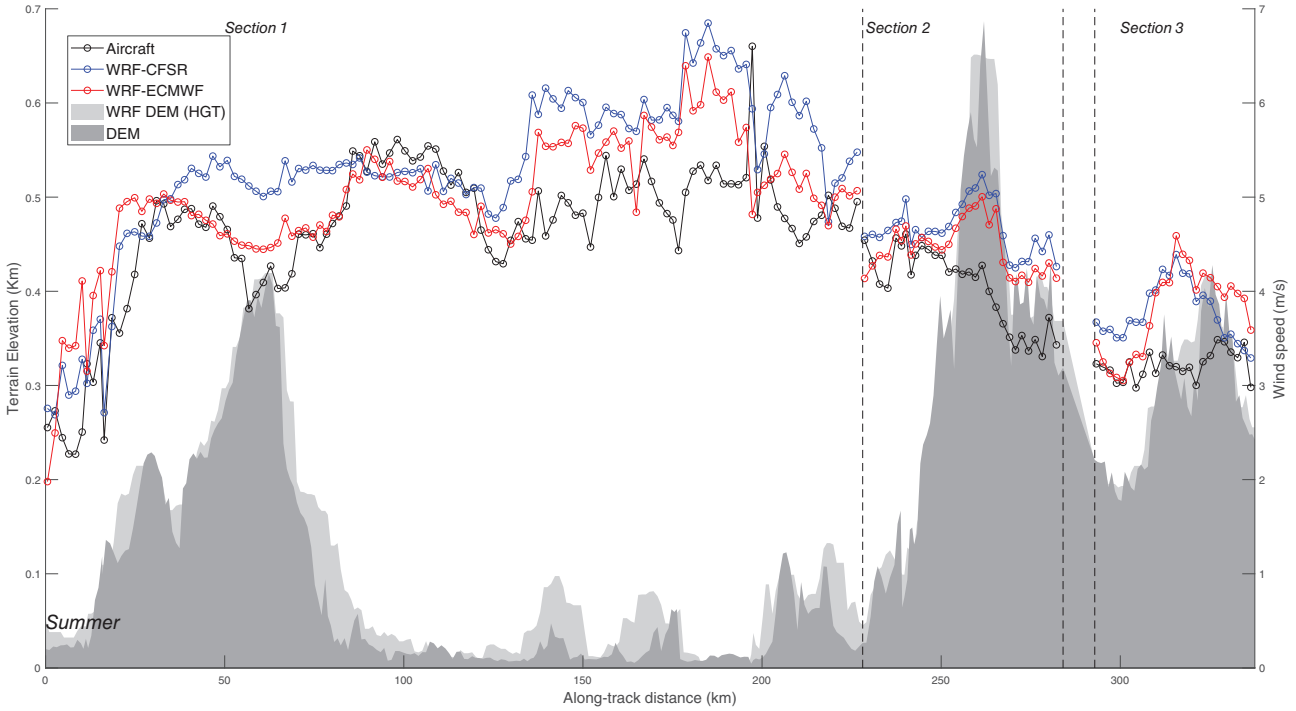

FIGURE 6 Spatialized wind speed for summer (season 3). Each solid line with circles indicates the wind speed (right *y*-axis) for a different data set: Aircraft (black), weather research and forecast (WRF) forced by the European Centre for Medium-Range Weather Forecasts (ECMWF) (WRF-ECMWF) (red) and the WRF-ARW forced by the Climate Forecast System Reanalysis (CFSR) (WRF-CFSR) (blue). Dark grey areas indicate terrain elevation (left *y*-axis) as *per* the Advanced Spaceborne Thermal Emission and Reflection Radiometer (ASTER) GDEM2, while the light grey areas show the WRF's own digital elevation model (HGT). Dashed black lines separate the sections

plotted against the mean distance from the coast. Figure 8 shows a non-univocal trend for the error of wind magnitude estimation when moving away from the coastline, which changes between forcings and seasons.

Finally, the significant discrepancies highlighted between the WRF model and measurements in section 3 (Figures 4–7), where there is a higher terrain elevation, are investigated in Figure 9. It compares the 20 km radius variance in the DEM with wind speed RMSEs for the different forcings of the WRF, highlighting, as *per* the coastline distance (Figure 8), a non-univocal trend between the RMSEs and the variation in elevation. Variance of the DEM and wind speed RMSEs is been binned into eight equally spaced bins. The highest RMSEs are found in correspondence with high DEM variances, indicating that a terrain with significant changes in orography affects the accuracy of wind speed computation.

4 | DISCUSSION

Among the two different reanalyses used in the study to drive WRF simulations, the ECMWF ERA-Interim has a comparable performance with the CFSR despite a coarser spatial resolution. A better performance of the ERA-Interim for wind speed estimation in comparison with ground observations was instead found by Lindsay *et al.* (2014). Such a reanalysis showed better performance at intermediate wind speeds (between 4 and 12 $m \cdot s^{-1}$), and the presence of a small counter clockwise rotation (Carvalho *et al.*, 2014). Bao and Zhang (2013) also compared the ERA-Interim and CFSR against independent soundings on the Tibetan Plateau and found a comparable RMSE between the two reanalyses and the soundings, corroborating the present findings. Yver *et al.* (2013) compared the ECMWF ERA-Interim and the NCEP-North America Model (NAM) data set, which is not a reanalysis but a forecast at 12 km resolution. Therefore, they compared a data set with a lower spatial resolution but higher accuracy (ECMWF ERA-Interim) with a more resolute but less accurate forecast (NCEP-NAM), and found that the ECMWF reanalysis better simulated wind at various ground stations. The results presented herein are in accordance with the cited literature: the WRF-ECMWF and WRF-CFSR both reported overall relatively low RMSEs for wind speed (Figure 2a) and good frequency correlations for wind direction (Table 3).

A further factor that could affect the errors between the model and the measurements could be the selection

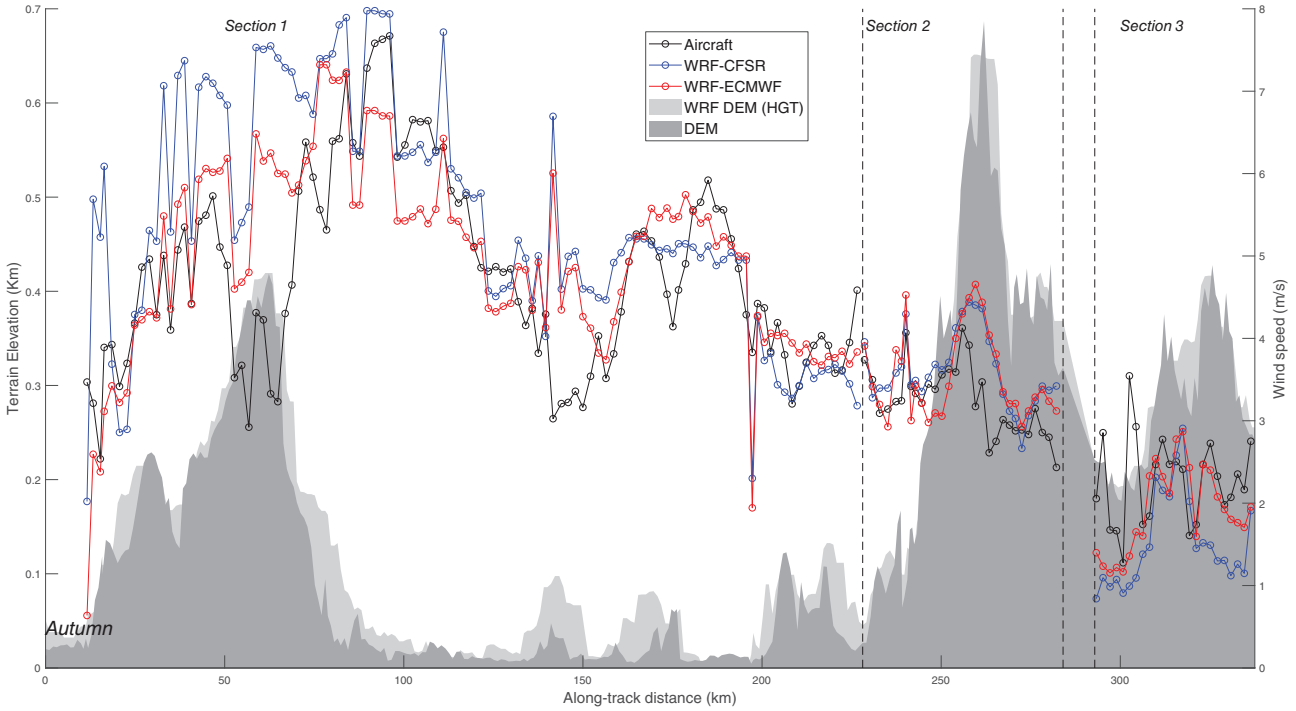

FIGURE 7 Spatialized wind speed for autumn (season 4). Each solid line with circles indicates the wind speed (right *y*-axis) for a different data set: Aircraft (black), weather research and forecast (WRF) forced by the European Centre for Medium-Range Weather Forecasts (ECMWF) (WRF-ECMWF) (red) and the WRF forced by the Climate Forecast System Reanalysis (CFSR) (WRF-CFSR) (blue). Dark grey areas indicate terrain elevation (left *y*-axis) as *per* the Advanced Spaceborne Thermal Emission and Reflection Radiometer (ASTER) GDEM2, while the light grey areas show the WRF's own digital elevation model (HGT). Dashed black lines separate the sections

of the model parameterization schemes. Yver *et al*. (2013) tested both different initial and boundary conditions and also different PBL schemes, concluding that the difference between the two initial and boundary conditions (ERA-Interim and NCEP-NAM) was larger than the differences between the various PBL schemes and, therefore, that the choice of the forcing had a greater impact on the simulated wind than the choice of the PBL scheme. Therefore, it is possible to assume that while parameterization schemes play a role in the model outputs, their effect is overwhelmed by the selection of the reanalysis.

Figure 3 shows that WRF reproduces the spatialized diurnal courses for wind speed with good accuracy with a few exceptions. These findings are particularly useful since, when the reanalysis was compared "as is" with flux tower data (Decker *et al*., 2012), no good correlations in wind speed between the towers and the data set were found on a diurnal time scale. Apparently, by employing a dynamical downscaling and a comparison with spatialized aircraft data, new information may be drawn by reanalysis data. Still a marked drop in wind speed r^2 occurs in all sections in summer and particularly in section 3, and in section 2 in autumn (when considering the daily courses Figure 3). This behaviour in summer likely reveals the presence of local thermal effects. Especially during warm periods, in fact, the complex orography may affect wind speed daily courses because of the formation of anabatic/katabatic effects (where the air mass close to the elevated ground is warmer/colder than the free air above (Papanastasiou *et al*., 2010).

Discrepancies in wind magnitude estimation do exist also in section 1 in parts of the track where there is no relevant terrain elevation (Figures 1b and 4–7). These discrepancies may be ascribed to breeze regimes: the misrepresentation of wind speed magnitude during a sea breeze with the WRF was reported, among others, by Hernández-Ceballos *et al*. (2013) while simulating breeze conditions in the Guadalquivir Valley. The aircraft data set presented here was used by Gioli *et al*. (2014) to validate a modelling chain using the WRF (Non-Hydrostatic Mesoscale Model v.2.1 initialized with the NCEP-GFS) and CALMET (Scire *et al*., 2000), and a similar influence of the breeze regime was also reported. In that work, the largest differences were observed in coastal areas in summer where breeze regimes develop consistently. A potential effect of breeze regimes on the wind speed simulated by the WRF is shown in Figure 8, where the wind speed RMSE was calculated along a transect from the coast to inland. In both winter and summer, both

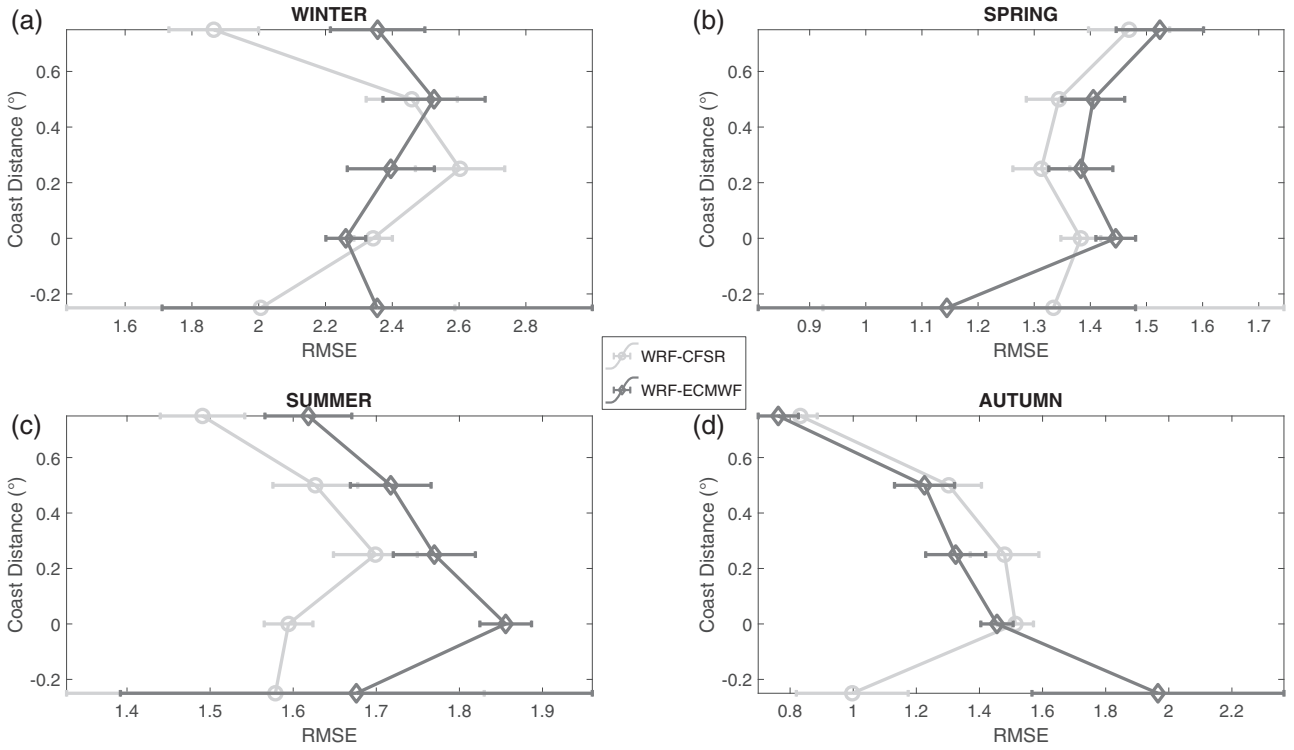

FIGURE 8 Effects of distance from the coast on the root mean square error (RMSE) of weather research and forecast (WRF)-simulated wind speed in various seasons: (a) winter; (b) spring; (c) summer; and (d) autumn. The dark grey line with diamonds indicates the RMSE of the WRF forced by the European Centre for Medium-Range Weather Forecasts (ECMWF) (WRF-ECMWF); and the light grey line with circles indicates the RMSE of the WRF forced by the Climate Forecast System Reanalysis (CFSR) (WRF-CFSR). Error bars show the standard error of the mean for averaged RMSEs

the WRF-ECMWF and the WRF-CFSR RMSEs wind patterns tend to increase and then decrease proceeding inland, likely representing the breeze penetration and confirming the presence of a winter sea breeze over the Tyrrhenian coasts (Ferretti *et al.*, 2003). A similar trend is identified by the WRF-CFSR in August, while the WRF-ECMWF shows a continuous decrease of the RMSE with distance from the coast. The spring pattern instead, where model data tend to underestimate measurements in section 1 (Figure 5), shows a general increase of the RMSE with an increase in the distance from the coast.

While in section 2 in winter both forcings exhibit a moderate r^2 between elevation and wind speed (WRF-ECMWF $r^2 = 0.33$, WRF-CFSR $r^2 = 0.36$), various situations show a decoupling between the measured and modelled wind speeds, such as some mountainous areas where the r^2 for both forcings was < 0.1. These effects may be driven by the WRF's DEM orographic smoothing impacting wind speed magnitude (Carvalho *et al.*, 2014): modelled data cannot quite "follow" the changes in velocity over the track because of the interactions between orography and air movement (e.g. changes in Froude number). When the interaction with orography results in an abatement of wind intensity, the model tends to overestimate such abatement (Figures 4, 6 and 7); conversely, when the measurements report a peak in intensity, the model tends to underestimate such increases (Figure 5). Figure 9 shows the relationship between the RMSE of the modelled *versus* the observed wind speed and five classes of DEM variance (calculated in a 20 km buffer around the selected DEM point): above a certain threshold (around 3,000 m), the RMSE tends to increase with variance, hinting to the aforementioned orographic effects. A similar effect is visible also for wind direction where both the WRF forcings show the highest drop in frequency correlation in section 2, which has the most significant orography. Employing finer subgrid-scale parameterization schemes could, in fact, improve the biases and errors because of the complex terrain (Yang and Duan, 2016).

Besides the effect of terrain elevation, different land uses may also affect the bias between modelled and measured data. The WRF default land use is based on a static data set derived from the MODIS, with fixed values for parameters such as roughness height, leaf area index and so on. Land-use categories are then aggregated to the domain resolution from their original 30 arcsec horizontal resolution. Given the limited number of land-use

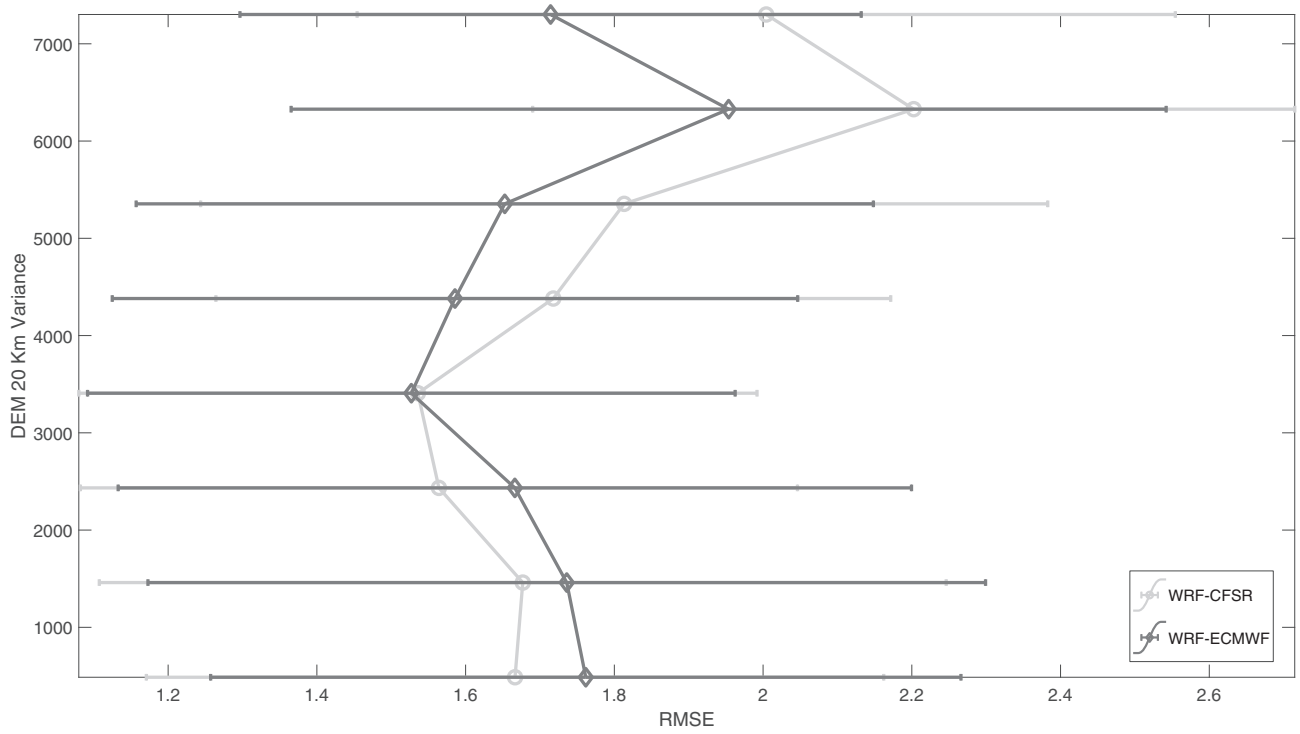

FIGURE 9 Effects of the digital elevation model (DEM) 20 km variance over the root mean square error (RMSE) of wind speed as simulated by the weather research and forecast (WRF) forced with the European Centre for Medium-Range Weather Forecasts (ECMWF) (WRF-ECMWF) (dark grey line with diamonds) and the Climate Forecast System Reanalysis (CFSR) (WRF-CFSR) (light grey line with circles). Error bars represent the standard error of the binned RMSEs

classes (see Section 2.1), their spatial aggregation and the fact that land use changes dynamically in reality (European Environmental Agency Report No. 10/2017[2]), this may affect the model's performance. Li *et al*. (2020), for example, forced the WRF with a new land-use data set based on the latest Global Land Cover Data set (GLC2015) at 300 m resolution and observed an improvement in the simulation of heat fluxes, wind and temperature at the surface. Similar results were also obtained by Nahian *et al*. (2020) when improving the land-use and topographical data set, highlighting the importance of considering land use as a physical driver of the biosphere atmosphere interaction rather than a static variable.

5 | CONCLUSIONS

In this study, the weather research and forecast (WRF) model was initialized with different forcings (European Centre for Medium-Range Weather Forecasts (ECMWF) ERA-Interim and National Centers for Environmental Predictions (NCEP) Climate Forecast System Reanalysis (CFSR)) on a domain that included both coastal areas and inland areas, and various degrees of terrain elevation, and simulated wind fields were compared with high-resolution aircraft data along a fixed route spanning multiple seasons.

Both forcings showed similar trends and were generally well capable of reproducing the spatialized observations. Wind speed showed overall good agreement with relatively small root mean square errors (RMSEs). Wind direction also showed a good frequency correlation, but while the trend was well captured, it showed the greatest fluctuations around the actual values. While there were certain situations (i.e. sections or seasons or daily courses) where one forcing showed marginally better statistics, no evidence was found that the WRF-ECMWF was overall always better than the WRF-CFSR.

While analysing spatialized data in different intensive observation periods (IOPs) across the various seasons, it was found that the model's performance was linked to the combination of both temporal and spatial effects, such as the presence of orography and the development of sea breeze regimes, that are convoluted in a complex manner. This poses a clear caveat when validating models only against point-based observations, since both their position and the chosen period may affect the model's performance. Aircraft data provide an additional

level of information at higher elevation and along specific transects that can improve mesoscale model performance assessment.

ACKNOWLEDGEMENTS

The authors thank Paolo Amico for piloting the Sky Arrow aircraft during the sampling campaigns presented in this study. The authors declare no conflict of interests. B. G. and P. T. designed and managed the experiments contributing to the conceptualization; B. G. and F. C. analysed the data contributing to data curation and formal analysis; B. G. also contributed to the supervision of the process; F. M. contributed to the funding acquisition; B. G., P. T. and G. G. contributed extensively to the writing of the paper and its review, which was co-ordinated by F. C.

ORCID

Federico Carotenuto https://orcid.org/0000-0001-9134-3073

ENDNOTES

[1]See https://asterweb.jpl.nasa.gov/gdem.asp/.

[2]See https://www.eea.europa.eu/publications/landscapes-in-transition/.

REFERENCES

Bao, X. and Zhang, F. (2013) Evaluation of NCEP-CFSR, NCEP-NCAR, ERA-Interim, and ERA-40 reanalysis datasets against independent sounding observations over the Tibetan plateau. *Journal of Climate*, 26, 206–214. https://doi.org/10.1175/JCLI-D-12-00056.1.

Bei, N., Li, G., Zavala, M., Barrera, H., Torres, R., Grutter, M., Gutiérrez, W., García, M., Ruiz-Suarez, L.G., Ortinez, A., Guitierrez, Y., Alvarado, C., Flores, I. and Molina, L.T. (2013) Meteorological overview and plume transport patterns during Cal-Mex 2010. *Atmospheric Environment*, 70, 477–489. https://doi.org/10.1016/j.atmosenv.2012.01.065.

Bonin, T.A., Chilson, P.B., Zielke, B.S., Klein, P.M. and Leeman, J. R. (2013) Comparison and application of wind retrieval algorithms for small unmanned aerial systems. *Geoscientific Instrumentation, Methods and Data Systems*, 2, 177–187. https://doi.org/10.5194/gi-2-177-2013.

Carvalho, D., Rocha, A., Gómez-Gesteira, M. and Silva Santos, C. (2014) WRF wind simulation and wind energy production estimates forced by different reanalyses: comparison with observed data for Portugal. *Applied Energy*, 117, 116–126. https://doi.org/10.1016/j.apenergy.2013.12.001.

Crawford, T.L. and Dobosy, R.J. (1992) A sensitive fast-response probe to measure turbulence and heat flux from any airplane. *Boundary-Layer Meteorology*, 59, 257–278.

de Foy, B., Burton, S.P., Ferrare, R.A., Hostetler, C.A., Hair, J.W., Wiedinmyer, C. and Molina, L.T. (2011) Aerosol plume transport and transformation in high spectral resolution lidar measurements and WRF-Flexpart simulations during the MILAGRO field campaign. *Atmospheric Chemistry and Physics*, 11, 3543–3563. https://doi.org/10.5194/acp-11-3543-2011.

Decker, M., Brunke, M.A., Wang, Z., Sakaguchi, K., Zeng, X. and Bosilovich, M.G. (2012) Evaluation of the reanalysis Products from GSFC, NCEP, and ECMWF using flux tower observations. *Journal of Climate*, 25, 1916–1944. https://doi.org/10.1175/jcli-d-11-00004.1.

Dee, D.P., Uppala, S.M., Simmons, A.J., Berrisford, P., Poli, P., Kobayashi, S., Andrae, U., Balmaseda, M.A., Balsamo, G., Bauer, P., Bechtold, P., Beljaars, A.C.M., van de Berg, L., Bidlot, J., Bormann, N., Delsol, C., Dragani, R., Fuentes, M., Geer, A.J., Haimberger, L., Healy, S.B., Hersbach, H., Hólm, E. V., Isaksen, L., Kållberg, P., Köhler, M., Matricardi, M., McNally, A.P., Monge-Sanz, B.M., Morcrette, J.J., Park, B.K., Peubey, C., de Rosnay, P., Tavolato, C., Thépaut, J.N. and Vitart, F. (2011) The ERA-Interim reanalysis: configuration and performance of the data assimilation system. *Quarterly Journal of the Royal Meteorological Society*, 137, 553–597. https://doi.org/10.1002/qj.828.

Doherty, R.M., Heal, M.R., Wilkinson, P., Pattenden, S., Vieno, M., Armstrong, B., Atkinson, R., Chalabi, Z., Kovats, S., Milojevic, A. and Stevenson, D.S. (2009) Current and future climate- and air pollution-mediated impacts on human health. *Environmental Health*, 8, S8. https://doi.org/10.1186/1476-069x-8-s1-s8.

Draxl, C., Hahmann, A.N., Peña, A. and Giebel, G. (2014) Evaluating winds and vertical wind shear from weather research and forecasting model forecasts using seven planetary boundary layer schemes. *Wind Energy*, 17, 39–55. https://doi.org/10.1002/we.1555.

Ek, M.B., Mitchell, K.E., Lin, Y., Rogers, E., Grunmann, P., Koren, V., Gayno, G. and Tarpley, J.D. (2003) Implementation of Noah land surface model advances in the National Centers for environmental prediction operational mesoscale eta model. *Journal of Geophysical Research: Atmospheres*, 108(D22), 12-1–12-16. https://doi.org/10.1029/2002JD003296.

Ferretti, R., Mastrantonio, G., Argentini, S., Santoleri, R. and Viola, A. (2003) A model-aided investigation of winter thermally driven circulation on the Italian Tyrrhenian coast: a case study. *Journal of Geophysical Research: Atmospheres*, 108(D24). https://doi.org/10.1029/2003JD003424.

García-Díez, M., Fernández, J., San-Martín, D., Herrera, S. and Gutiérrez, J.M. (2015) Assessing and improving the local added value of the WRF for wind downscaling. *Journal of Applied Meteorology and Climatology*, 54, 1556–1568. https://doi.org/10.1175/jamc-d-14-0150.1.

Giannaros, T.M., Melas, D. and Ziomas, I. (2017) Performance evaluation of the weather research and forecasting (WRF) model for assessing wind resource in Greece. *Renewable Energy*, 102, 190–198. https://doi.org/10.1016/j.renene.2016.10.033.

Gioli, B., Gualtieri, G., Busillo, C., Calastrini, F., Gozzini, B. and Miglietta, F. (2014) Aircraft wind measurements to assess a coupled WRF-CALMET mesoscale system. *Meteorological Applications*, 21, 117–128. https://doi.org/10.1002/met.1419.

Gioli, B., Miglietta, F., Vaccari, F.P., Zaldei, A. and De Martino, B. (2006) The sky arrow ERA, an innovative airborne platform to monitor mass, momentum and energy exchange of ecosystems. *Annals of Geophysics*, 49, 109–116. https://doi.org/10.4401/ag-3159.

Grell, G., Fast, J., Gustafson, W.I., Peckham, S.E., McKeen, S., Salzmann, M. and Freitas, S. (2011) On-line chemistry within WRF: description and evaluation of a state-of-the-art multiscale air quality and weather prediction model. In: Baklanov, A., Alexander, M. and Sokhi, R. (Eds.) *Integrated Systems of Meso-Meteorological and Chemical Transport Models*. Berlin, Heidelberg: Springer, pp. 41–54. https://doi.org/10.1007/978-3-642-13980-2_3.

Grell, G.A., Dudhia, J., Stauffer, D.R., (1994). A description of the fifth-generation Penn State/NCAR mesoscale model (MM5). *NCAR Tecehnical Note NCAR/TN-398+STR* 121. https://doi.org/10.5065/D60Z716B

Hernández-Ceballos, M.A., Adame, J.A., Bolívar, J.P. and De la Morena, B.A. (2013) A mesoscale simulation of coastal circulation in the Guadalquivir valley (southwestern Iberian Peninsula) using the WRF-ARW model. *Atmospheric Research*, 124, 1–20. https://doi.org/10.1016/j.atmosres.2012.12.002.

Hong, S.-Y., Noh, Y. and Dudhia, J. (2006) A new vertical diffusion package with an explicit treatment of entrainment processes. *Monthly Weather Review*, 134, 2318–2341.

Iacono, M.J., Delamere, J.S., Mlawer, E.J., Shephard, M.W., Clough, S.A. and Collins, W.D. (2008) Radiative forcing by long-lived greenhouse gases: calculations with the AER radiative transfer models. *Journal of Geophysical Research: Atmospheres*, 113(D13), 1–8.

ISPRA. (2010) *La Realizzazione in Italia del Progetto Corine Land Cover*, Vol. 2006, Roma (Italy): Istituto Superiore per la Protezione e la Ricerca Ambientale (ISPRA).

Jiménez, P.A. and Dudhia, J. (2013) On the ability of the WRF model to reproduce the surface wind direction over complex terrain. *Journal of Applied Meteorology and Climatology*, 52, 1610–1617. https://doi.org/10.1175/jamc-d-12-0266.1.

Jiménez, P.A., Dudhia, J., González-Rouco, J.F., Montávez, J.P., García-Bustamante, E., Navarro, J., Vilà-Guerau de Arellano, J. and Muñoz-Roldán, A. (2013) An evaluation of the WRF's ability to reproduce the surface wind over complex terrain based on typical circulation patterns. *Journal of Geophysical Research: Atmospheres*, 118, 7651–7669. https://doi.org/10.1002/jgrd.50585.

Jiménez, P.A., Dudhia, J., González-Rouco, J.F., Navarro, J., Montávez, J.P. and García-Bustamante, E. (2012) A revised scheme for the WRF surface layer formulation. *Monthly Weather Review*, 140, 898–918. https://doi.org/10.1175/mwr-d-11-00056.1.

Kocer, G., Mansour, M., Chokani, N., Abhari, R.S. and Müller, M. (2011) Full-scale wind turbine near-wake measurements using an instrumented uninhabited aerial vehicle. *Journal of Solar Energy Engineering*, 133, 41011–41018. https://doi.org/10.1115/1.4004707.

Li, H., Zhang, H., Mamtimin, A., Fan, S. and Ju, C. (2020) A new land-use dataset for the weather research and forecasting (WRF) model. *Atmosphere*, 11(4), 1–18. https://doi.org/10.3390/atmos11040350.

Lindsay, R., Wensnahan, M., Schweiger, A. and Zhang, J. (2014) Evaluation of seven different atmospheric reanalysis products in the Arctic. *Journal of Climate*, 27, 2588–2606. https://doi.org/10.1175/jcli-d-13-00014.1.

Maselli, F., Gioli, B., Chiesi, M., Vaccari, F., Zaldei, A., Fibbi, L., Bindi, M. and Miglietta, F. (2010) Validating an integrated strategy to model net land carbon exchange against aircraft flux measurements. *Remote Sensing of Environment*, 114, 1108–1116. https://doi.org/10.1016/j.rse.2009.12.023.

Mayer, S., Hattenberger, G., Brisset, P., Jonassen, M.O. and Reuder, J. (2012) A 'no-flow-sensor' wind estimation algorithm for unmanned aerial systems. *International Journal of Micro Air Vehicles*, 4, 15–29. https://doi.org/10.1260/1756-8293.4.1.15.

Miglietta, F., Gioli, B., Hutjes, R.W.A. and Reichstein, M. (2007) Net regional ecosystem CO2 exchange from airborne and ground-based eddy covariance, land-use maps and weather observations. *Global Change Biology*, 13, 548–560. https://doi.org/10.1111/j.1365-2486.2006.01219.x.

Mlawer, E.J., Taubman, S.J., Brown, P.D., Iacono, M.J. and Clough, S.A. (1997) Radiative transfer for inhomogeneous atmospheres: RRTM, a validated correlated-k model for the longwave. *Journal of Geophysical Research: Atmospheres*, 102, 16663–16682.

Mohan, M. and Bhati, S. (2011) Analysis of the WRF model performance over subtropical region of Delhi, India. *Advances in Meteorology*, 2011, 1–13. https://doi.org/10.1155/2011/621235.

Morrison, H., Thompson, G. and Tatarskii, V. (2009) Impact of cloud microphysics on the development of trailing stratiform precipitation in a simulated squall line: comparison of one- and two-moment schemes. *Monthly Weather Review*, 137, 991–1007.

Nahian, M.R., Nazem, A., Nambiar, M.K., Byerlay, R., Mahmud, S., Aliabadi, A.A., Seguin, A.M., Robe, F.R. and Ravenhill, J. (2020) Complex meteorology over a complex mining facility: assessment of topography, land use, and grid spacing modifications in WRF. *Journal of Applied Meteorology and Climatology*, 59(4), 769–789. https://doi.org/10.1175/JAMC-D-19-0213.1.

Nehrkorn, T., Henderson, J., Leidner, M., Mountain, M., Eluszkiewicz, J., McKain, K. and Wofsy, S. (2013) WRF simulations of the urban circulation in the Salt Lake City area for CO2 modeling. *Journal of Applied Meteorology and Climatology*, 52, 323–340. https://doi.org/10.1175/jamc-d-12-061.1.

Papanastasiou, D.K., Melas, D. and Lissaridis, I. (2010) Study of wind field under sea breeze conditions; an application of the WRF model. *Atmospheric Research*, 98, 102–117. https://doi.org/10.1016/j.atmosres.2010.06.005.

Reuder, J., Jonassen, M. and Ólafsson, H. (2012) The small unmanned meteorological observer SUMO: recent developments and applications of a micro-UAS for atmospheric boundary layer research. *Acta Geophysica*, 60(5), 1454–1473. https://doi.org/10.2478/s11600-012-0042-8.

Saha, S., Moorthi, S., Pan, H.-L., Wu, X., Wang, J., Nadiga, S., Tripp, P., Kistler, R., Woollen, J., Behringer, D., Liu, H., Stokes, D., Grumbine, R., Gayno, G., Wang, J., Hou, Y.-T., Chuang, H., Juang, H.-M.H., Sela, J., Iredell, M., Treadon, R., Kleist, D., Van Delst, P., Keyser, D., Derber, J., Ek, M., Meng, J., Wei, H., Yang, R., Lord, S., van den Dool, H., Kumar, A., Wang, W., Long, C., Chelliah, M., Xue, Y., Huang, B., Schemm, J.-K., Ebisuzaki, W., Lin, R., Xie, P., Chen, M., Zhou, S., Higgins, W., Zou, C.-Z., Liu, Q., Chen, Y., Han, Y., Cucurull, L., Reynolds, R.W., Rutledge, G. and Goldberg, M. (2010) The NCEP climate forecast system reanalysis. *Bulletin of the American Meteorological Society*, 91, 1015–1058. https://doi.org/10.1175/2010BAMS3001.1.

Saide, P.E., Carmichael, G.R., Spak, S.N., Gallardo, L., Osses, A.E., Mena-Carrasco, M.A. and Pagowski, M. (2011) Forecasting

urban PM10 and PM2.5 pollution episodes in very stable nocturnal conditions and complex terrain using WRF–Chem CO tracer model. *Atmospheric Environment*, 45, 2769–2780. https://doi.org/10.1016/j.atmosenv.2011.02.001.

Santos-Alamillos, F.J., Pozo-Vázquez, D., Ruiz-Arias, J.A., Lara-Fanego, V. and Tovar-Pescador, J. (2013) Analysis of the WRF model wind estimate sensitivity to physics parameterization choice and terrain representation in Andalusia (southern Spain). *Journal of Applied Meteorology and Climatology*, 52, 1592–1609.

Scire, J.S., Robe, F.R., Fernau, M.E. and Yamartino, R.J. (2000) *A User's Guide for the CALMET Meteorological Model*, Vol. 37. Menlo Park, CA: Earth Tech.

Simmons, A., Uppala, S.M., Dee, D.P. and Kobayashi, S. (2007) ERA-Interim: new ECMWF reanalysis products from 1989 onwards. *ECMWF Newsletter*, 110, 25–36. https://doi.org/10.21957/pocnex23c6.

Skamarock, W.C., Klemp, J.B., Dudhia, J., Gill, D.O., Barker, D. M., Duda, M.G., Huang, X.Y., Wang, W. and Powers, J.G. (2008) *A Description of the Advanced Research WRF Version 3, NCAR Technical Note, Mesoscale and Microscale Meteorology Division*. Boulder, CO: National Center for Atmospheric Research.

Tachikawa, T., Kaku, M., Iwasaki, A., Gesch, D.B., Oimoen, M.J., Zhang, Z., Danielson, J.J., Krieger, T., Curtis, B., Haase, J., Abrams, M., Carabajal, C., (2011). *ASTER Global Digital Elevation Model Version 2—Summary of Validation Results*.

Thomas, R.M., Lehmann, K., Nguyen, H., Jackson, D.L., Wolfe, D. and Ramanathan, V. (2012) Measurement of turbulent water vapor fluxes using a lightweight unmanned aerial vehicle system. *Atmospheric Measurement Techniques*, 5, 243–257. https://doi.org/10.5194/amt-5-243-2012.

Toscano, P., Gioli, B., Dugheri, S., Salvini, A., Matese, A., Bonacchi, A., Zaldei, A., Cupelli, V. and Miglietta, F. (2011) Locating industrial VOC sources with aircraft observations. *Environmental Pollution*, 159, 1174–1182. https://doi.org/10.1016/j.envpol.2011.02.013.

Vellinga, O.S., Dobosy, R.J., Dumas, E.J., Gioli, B., Elbers, J.A. and Hutjes, R.W.A. (2013) Calibration and quality Assurance of Flux Observations from a small research aircraft. *Journal of Atmospheric and Oceanic Technology*, 30, 161–181. https://doi.org/10.1175/JTECH-D-11-00138.1.

Waked, A., Seigneur, C., Couvidat, F., Kim, Y., Sartelet, K., Afif, C., Borbon, A., Formenti, P. and Sauvage, S. (2013) Modeling air pollution in Lebanon: evaluation at a suburban site in Beirut during summer. *Atmospheric Chemistry and Physics*, 13, 5873–5886. https://doi.org/10.5194/acp-13-5873-2013.

Wharton, S., Simpson, M., Osuna, J., Newman, J. and Biraud, S. (2013) *Assessment of Land Surface Model Performance in WRF for Simulating Wind at Heights Relevant to the Wind Energy Community*. Livermore, CA: Lawrence Livermore National Laboratory (LLNL). https://doi.org/10.2172/1097768.

Yang, F., Pan, H.-L., Krueger, S.K., Moorthi, S. and Lord, S.J. (2006) Evaluation of the NCEP global forecast system at the ARM SGP site. *Monthly Weather Review*, 134, 3668–3690. https://doi.org/10.1175/mwr3264.1.

Yang, J. and Duan, K. (2016) Effects of initial drivers and land use on WRF modeling for near-surface fields and atmospheric boundary layer over the northeastern Tibetan plateau. *Advances in Meteorology*, 2016, 7849249. https://doi.org/10.1155/2016/7849249.

Yang, Q., Berg, L.K., Pekour, M., Fast, J.D., Newsom, R.K., Stoelinga, M. and Finley, C. (2013) Evaluation of the WRF-predicted near-hub-height winds and ramp events over a Pacific northwest site with complex terrain. *Journal of Applied Meteorology and Climatology*, 52, 1753–1763. https://doi.org/10.1175/JAMC-D-12-0267.1.

Yuan, R., Ji, W., Luo, K., Wang, J., Zhang, S., Wang, Q., Fan, J., Ni, M. and Cen, K. (2017) Coupled wind farm parameterization with a mesoscale model for simulations of an onshore wind farm. *Applied Energy*, 206, 113–125. https://doi.org/10.1016/j.apenergy.2017.08.018.

Yver, C.E., Graven, H.D., Lucas, D.D., Cameron-Smith, P.J., Keeling, R.F. and Weiss, R.F. (2013) Evaluating transport in the WRF model along the California coast. *Atmospheric Chemistry and Physics*, 13, 1837–1852. https://doi.org/10.5194/acp-13-1837-2013.

SUPPORTING INFORMATION

Additional supporting information may be found online in the Supporting Information section at the end of this article.

How to cite this article: Carotenuto F, Gualtieri G, Toscano P, Miglietta F, Gioli B. WRF wind field assessment under multiple forcings using spatialized aircraft data. *Meteorol Appl*. 2020; 27:e1920. https://doi.org/10.1002/met.1920